Indonesian Journal of Aerospace Vol. 24 No. 1 June 2026 : pp 73–90 (Wuwung et al.)
DOI: 10.55981/ijoa.2026.15509
https://ejournal.brin.go.id/ijoa/

Numerical Investigation of Propeller Vibration due to Propeller Performance and Blade Angle Effect

Vicky Wuwung, Zaim Sidqi Islami*, Ismi Damaiyanti, Yohanes Sinung Nugroho, Teguh Wibowo, Radi Suradi Kartanegara

Department of Aeronautical Engineering, Faculty of Mechanical Engineering, Bandung State Polytechnic, Jl. Gegerkalong Hilir, Ciwaruga, Kec. Parongpong, Bandung Barat, 40559, Indonesia
*e-mail: zaim.sidqi@polban.ac.id

Received: 30/07/2025 Revised: 07/02/2026 Accepted: 27/02/2026 Published: 26/10/2026

Abstract

The propeller is an essential component of an aircraft that generates thrust. It must be capable of withstanding significant loads at its hub due to centrifugal, thrust, and tangential forces. Among these forces, centrifugal force can cause vibrations during high-frequency engine rotation. Excessive speeds at the propeller blade tips (resulting in shockwaves) can also lead to vibrations. Continuous vibrations as the propeller speed increases can cause fatigue in the propeller structure. Therefore, it is necessary to analyze the effect of propeller speed on vibrations. Numerical simulation methods are employed to determine the propeller speed at which vibrations occur. The numerical simulation performed involves Fluid-Structure Interaction (FSI) in unsteady conditions using modal approach and nonlinear harmonic method. From the numerical simulation results, performance curves for each propeller angle are obtained. The highest efficiency value at an angle of 18° is 0.39 at 1736 RPM. In contrast, angles of 20° and 22° have efficiency values of 0.59 and 0.68, respectively, at 1936 RPM. The vibration characteristics were then analyzed at those conditions when the efficiency is at the highest value. The maximum deformations observed for each angle are 0.183 mm, 0.185 mm, and 0.187 mm. with vibration velocity 8.17 x 10-6 mm/s. There is no rapid increase on deformation in short period of time, which means there are no indication of flutter. Also considering the vibration acceptable limit of 0.2 IPS (5.08 mm/s), the propeller operation can be considered safe.

Keywords: *propeller, modal approach, nonlinear harmonics, fluid structure interaction, vibration*

Nomenclature

$[M]$	=	Mass matrix	P	=	Propeller Power (W)
$[C]$	=	Damping matrix	V	=	Airspeed (km/h)
$[K]$	=	Stiffness Matrix	n	=	Rotational speed (rev / s)
F	=	force, N	D	=	Propeller Diameter (m)
$\vec{d}$	=	Displacement of the structure	C_T	=	Thrust Coefficient
$\vec{f}$	=	External load	C_P	=	Power Coefficient
T	=	Propeller Thrust (N)	J	=	Propeller Advance Ratio
Q	=	Propeller Torque (Nm)	η	=	Propeller Efficiency
ω	=	Natural /eigenfrequency (rad/s)	$\vec{\emptyset}$	=	Mode shape vector / eigenvector
λ	=	Eigen value	q	=	Generalized displacement (m)
ξ	=	Damping coefficient	f	=	Generalized load (N)
U	=	Conservative flow variable	F_c, F_v	=	Convective & Viscous Flux
$\vec{S}$	=	Surface unit vector	$D_{x,y,z}$	=	Strain terms
S_T	=	Source terms	Ω	=	Volume terms

e-ISSN 2597-7873 (online) | © 2026 The Author(s). Published by BRIN Publishing.
This is an open access article under the CC BY-SA license(https://creativecommons.org/licenses/by-sa/4.0/)
IJOA accredited as Sinta 2 Journal (https://sinta.kemdikbud.go.id/journals/profile/3362)

1. Introduction

A propeller is a component used to generate thrust in an aircraft by moving a mass of air backwards, thereby creating a force that helps propel the aircraft forward. It must be able to withstand significant force and moment at the hub caused by centrifugal force, thrust force, and tangential force. Of these forces, the primary force is centrifugal force. The high rotational speed of shaft may lead to excessive wear on bearing, which may introduce imbalance and promote vibration on the system (Muetze & Strangas, 2016). Excessive friction in the pitch change mechanism may lead to sudden increases in RPM or torque(Saputra & Hakim, 2018). Therefore, it is important to understand the vibration characteristics produced by variations in propeller rotational speeds.

An analysis of an efficient and accurate propeller using a hybrid numerical Navier-Stokes/ Free-wake method showed a very good correlation with the measured data and at least as good correlation as the full Navier-Stokes simulation.(Min et al., 2015; Czyz et al., 2021). High fidelity CFD methods using unsteady flow modeling and LES (Large Eddy Simulation) are also performed on propeller stall flutter, including the effect of modifications like the addition of winglet (Higgins et al., 2019; Zhu & Gao, 2019).

Structural simulation of vibrating propellers compares aluminum and composite as the material, showing differences in deflection and natural frequency, while affecting the vibration characteristics and applied stress under operational loads (Prasad L, et al., 2018). Additionally, vibration-based monitoring can be developed to detect potential structural faults on the system, assisting in maintenance and safety considerations (Ghalamchi & Mueller, 2018; Qu et al, 2017). Propellers that have high natural frequency may imply higher resonance resistance on flight operations (Ruseno, 2024). Therefore, it is important to understand the vibration characteristics produced by variations in propeller rotational speeds.

2. Methodology

This research method follows the flowchart as depicted in (Figure 2-1).

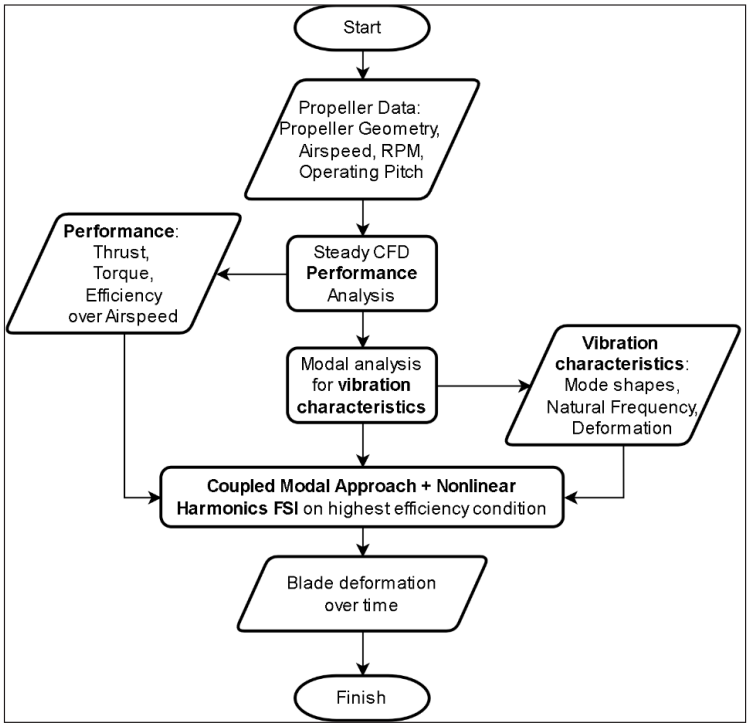


Figure 2-1: Research Flowchart

The Vibration analysis of the propeller is performed using numerical simulation, especially Fluid Structure Interaction (FSI). The CFD analysis is performed using Numeca software, which is performed after determining the mode shapes and natural frequency of the geometry using PERMAS. The order of simulation in this study is determining propeller geometry, computing the propeller performance on NUMECA CFD, mode shape analysis for vibration characteristics on PERMAS, and lastly coupling the modal approach FEM and nonlinear harmonics CFD to compute the blade deformation on highest efficiency condition back to NUMECA using vibration characteristics generated on PERMAS.

2.1. Related Works

Aerodynamic study of 64 x 24 inch propeller was performed on 2000 to 3000 RPM. While the thrust value matches the factory specifications at 2000 RPM, the performance nearing 3000 RPM is much lower, possibly from compressibility effect or limited mesh issue (Mak, et al., 2022).

The cause of the Cessna 172 propeller problem was identified as excessive friction in the pitch change mechanism. If this leads to sudden increases in RPM or torque, the issue can be resolved by addressing the problem in the hub mechanism. The engine should be capable of purging air from the system during 1 1/2 rotations or cycles. This is done to overcome air pockets in the propeller motor and excessive movement prior to takeoff (Saputra, et al., 2016). An analysis of an efficient and accurate propeller using a hybrid numerical Navier-Stokes/ Free-wake method. The results showed a very good correlation with the measured data and at least as good correlation as the full Navier-Stokes simulation (Min, et al., 2015).

A study on propeller flutter using a developed aeroelastic time-marching method was conducted with the advancement of modern propeller design that potentially pushes the flutter boundaries and faster computational power development, computational fluid dynamics (CFD) is needed to ensure accurate capture of aerodynamics (Higgins, et al., 2019). Meanwhile, a study to evaluate the strength and vibration characteristics of propeller blade designs for both metal and composite materials was performed utilizing a 3D model of the propeller blade created using SOLID EDGE software. (Prasad, et al., 2018). The stress analysis revealed a maximum deflection of 22 mm for the aluminum material, while a deflection of 93 mm was observed for the composite material. The maximum stress in the metal was found to be 167 MPa, whereas in the composite material, it was 94 MPa, which is within the acceptable limits. Comparing the vibration analysis, the first bending mode occurred at 47.3 Hz for the metal propeller blade, whereas for the composite material, it was observed at 23.1 Hz (Prasad, et al., 2018).

A nonlinear vibration analysis was performed on a Marine cycloidal propeller considering variations in plate thickness and asymmetric support characteristics to account for the aerofoil section and stock support using nonlinear finite element method. To calculate the hydrodynamic loads, a simplified model was utilized. The analysis was performed using FEM software and ANSYS. However, both software packages had their limitations (Prabhu, et al., 2021). Aeroelastic behavior analysis of a Commander propeller blade using URANS method shows that the trailing edge vortex had a greater influence at 70% of the station, as the station was severely congested. This led to the separation of the stall bubble from that particular section, as observed at 1650, with a trailing edge vortex (Higgins, et al., 2021).

A flying wing rigid body 6DOF analysis predicts the flutter characteristics for high aspect ratio wing (Ji, et al., 2024). Meanwhile, Pazy wing model flutter tests are performed by entering and exiting limit-cycle oscillations (Drachinsky, et al., 2022). Both results shows that flutter occurs when the deformation rapidly diverges over a short time period in less than 5 seconds.

2.2. Problem Definition

Referring to those previous studies, this study will focus on the effect of propeller thrust, efficiency value and blade angle variation to the vibration characteristics namely natural frequency, amplitude, and eigenvalue for each mode shapes. Note that the amplitude will be scaled based on the load strength. The research objective is to review whether the vibration due to the propeller operation poses risks to the structural integrity, by analyzing the vibration deflection and speed and comparing it to the acceptable limits provided in the propeller manual.

2.3. Method

Propeller data consists of propeller geometry and performance, including the airfoil of each propeller section. The analyzed propeller data is Hartzell P/N 9349-6.5 obtained from Hartzell propeller maintenance manual with diameter of 87" (220.98 cm). After obtaining the geometry of the propeller, it is necessary to create models of the shroud and spinner to facilitate the numerical simulations that will be conducted. The propeller, shroud, and spinner models can be created using SolidWorks software. It is important to ensure that the dimensions of these models are consistent with the obtained propeller geometry.

Propeller vibration properties data is necessary to perform vibration simulation, which will be obtained using PERMAS software. The resulting vibration properties data will be mode shapes, natural frequencies, and deformation values of every grid element. The simulation settings are shown in (Table 2-1).

Table 2-1: Simulation settings

No	Criteria	Value
1	Propeller Pitch Angle	18°, 20°, and 22°
2	RPM	1536, 1636, 1736, 1836, and 1936
3	Inlet Airspeed (km/h)	0, 25, 50, 75, 80, and 85
4	Turbulence Model	Spalart-Allmaras
5	Fluid type	Air (Ideal Gas)
6	Pressure at 9000 ft (Inlet, Farfield)	72428 Pa
7	Temperature at 9000 ft (Inlet, Farfield)	270.2 K
8	y+ (Near wall treatment)	1
9	Total cell count (CFD)	2.5 million
10	Number of Mode shapes	10

Modal Coupling

Modal coupling approach is to compute the modal shapes and the eigen frequencies.

$$[M]\frac{\partial^2 \vec{d}}{\partial t^2} + [C]\frac{\partial \vec{d}}{\partial t} + [K]\vec{d} = \vec{f} \tag{2-1}$$

Fluid-Structure Interaction (FSI) defines external load as the aerodynamic force computed in Computational Fluid Dynamics (CFD). Considering undamped structure without load, Eq. 2-1 can be written as:

$$[M]\frac{\delta^2 \vec{d}}{\delta t^2} + [K]\vec{d} = \vec{0} \tag{2-2}$$

This equation has not trivial solution only if:

$$\mathrm{Det}([K] - \lambda[M]) = 0 \tag{2-3}$$

The eigenvalues of Eq. 2-3 lead to natural frequencies of the structure and natural mode shapes:

$$\omega_k = \sqrt{\lambda_k} \tag{2-4}$$

$$[K]\vec{\emptyset}_k = \lambda_k[M]\,\vec{\emptyset}_k \tag{2-5}$$

The global deformation of the structure can be written as a composition of these modes where $q_k q_k$ is the generalized displacement:

$$\vec{d} = \sum_{k=1}^{n_{\text{modes}}} q_k \vec{\phi}_k \tag{2-6}$$

Using Eq. 2-6 in the modal equation, assuming a Rayleigh damping, a stiffness frequency-independent and choosing a proper scale factor for the mode shape, we can get a set of independent equations for each mode kk where $\xi_k \xi_k$ is the damping coefficient for each mode shape:

$$\frac{\partial^2 q_k}{\partial t^2} + 2\xi_k \omega_k \frac{\partial q_k}{\partial t} + \omega_k^2 q_k = \vec{\phi}_k^T \vec{f} \tag{2-7}$$

If the load $\vec{f}\vec{f}$ is split into a relative load and a reference load (reference generalized aerodynamic forces), the right-hand term of the modal equation becomes:

$$\vec{\Phi}_k^T\left(\overrightarrow{f_{rel}} + \overrightarrow{f_{ref}}\right) = \vec{\Phi}_k^T \overrightarrow{f_{rel}} + GAF_{ref,k} \tag{2-8}$$

From the solver point of view, the load exerted by the fluid onto the structure is the total load. As the reference is already accounted for in the modal representation of the structure, it will be subtracted from the total generalized aerodynamic force (GAF) to only consider the relative GAF in the modal equation resolved.

For the coupled simulation, the mode equation is solved by the flow solver at each physical time step. After reconstruction with the equation of global deformation, it gives the new shape of the structure around which the flow is computed. In case of combining with the harmonic method, the mode equation is solved in the frequency domain every ITCPL iterations.

For the forced motion simulation, the generalized displacement q_k for each mode shape is specified by the user. The new shape of the structure is directly computed by the equation of global deformation. In case of combining with the harmonic method, the generalized displacement q_k is computed by:

$$q(t) = \bar{q} + \Sigma q'(t) \tag{2-9}$$

$$q'(t) = \sum_{i=1}^{N} \left(\tilde{q}_i e^{I\omega_i t} + \tilde{q}_{-i} e^{I\omega_{-i} t}\right)$$

Where $\bar{q}\bar{q}$ is the time mean value specified in the interface, $\tilde{q}_i = \tilde{q}_{i,R} + I\tilde{q}_{i,I}$ $\tilde{q}_i = \tilde{q}_{i,R} + I\tilde{q}_{i,I}$ with $\tilde{q}_{i,R}\tilde{q}_{i,R}$ the real part and $\tilde{q}_{i,I}\tilde{q}_{i,I}$ the imaginary part specified in the interface, $\tilde{q}_{-i}\tilde{q}_{-i}$ is the conjugate of the complex number $\tilde{q}_i\tilde{q}_i$.

In the trigonometrical form, the generalized displacement $q_k q_k$ can be written as:

$$q'(t) = \sum_{i=1}^{N} 2\left[\tilde{q}_{i,R}\cos(i\omega t) - \tilde{q}_{i,I}\sin(i\omega t)\right] \tag{2-10}$$

From the definition of the generalized displacement, the physical deformation is retrieved with a time-averaged term and the harmonic fluctuations:

$$\vec{\tilde{d}} = \sum_{k=1}^{n_{\text{modes}}} \overline{q_k}\overrightarrow{\phi_k}$$

$$\vec{\tilde{d}}_i = \sum_{k=1}^{n_{\text{modes}}} \left(\tilde{q}_{ik,R}\vec{\phi}_{k,R} - \tilde{q}_{ik,I}\vec{\phi}_{k,I}\right) + I\left(\tilde{q}_{ik,I}\vec{\phi}_{k,R} + \tilde{q}_{ik,R}\vec{\phi}_{k,I}\right) \tag{2-11}$$

In case of real mode shapes, the harmonic fluctuations can be simplified as $\vec{\phi}_{k,I} = 0$.

Nonlinear Harmonic Method

The Nonlinear Harmonic Method is used to calculate the structural vibrations. The unsteady Reynolds Averaged Navier-Stokes equations are considered, formulated in Cartesian coordinates (x,y,z) in a rotating frame for the conservative flow variable $U = (\rho, \overrightarrow{\rho v}, \rho E)$ where $\vec{v} = (v_x, v_y, v_z)$ is the relative velocity.

The conservative variable is decomposed into a time-averaged value and a sum of periodic perturbations, which in turn can be decomposed into NN harmonics:

$$U(\vec{r},t) = \bar{U}(\vec{r}) + \sum U'(r',t)$$

$$U'(\vec{r},t) = \sum_{k=1}^{N} \left(\tilde{U}_k(\vec{r})e^{I\omega_k t} + \tilde{U}_{-k}(\vec{r})e^{I\omega_{-k}t}\right) \tag{2-12}$$

The first harmonic being the fundamental associated with the blade passing frequency (BPF) of a blade row for instance. The harmonic amplitudes $\tilde{U}_k$ and $\tilde{U}_{-k}$ are complex conjugates.

A time-mean flow equation is obtained by time-averaging the unsteady equations. This is like Reynolds averaging, except that the unsteady perturbations are periodic fluctuations, assumed to be preponderant over the turbulent fluctuations. The resulting time-mean flow equations are in a conservative form and can be formulated following a finite-volume method as

$$\Omega_i \frac{d\bar{U}}{dt_i} = -\sum_{cellfaces} \bar{F}_c\vec{S} + \sum_{cellfaces} \bar{F}_v\vec{S} + \Omega_i\overline{S_{Ti}} \tag{2-13}$$

where i is the cell number and Ω_i its volume. F_c and F_v are respectively the discretized convective and viscous fluxes, and S_T is the source term that includes the Coriolis and centrifugal terms.

The nonlinearity makes the deterministic stress terms appear in the time-averaged equation in the same way as Reynolds stress terms appear in the Reynolds averaged equations. They provide new contributions $Det_c Det_c$ and $Det_v Det_v$ to the advective and viscous fluxes following:

$$\vec{F_v S} = \begin{bmatrix} 0 \\ \bar{D}_x \cdot \vec{S} \\ \bar{D}_y \cdot \vec{S} \\ \bar{D}_z \cdot \vec{S} \\ (B \cdot \vec{S}) + \bar{q} \end{bmatrix} + \begin{bmatrix} 0 \\ 0 \\ 0 \\ 0 \\ \mathrm{Det}_v \end{bmatrix} \tag{2-14}$$

where $D_x = (\tau_{xx}, \tau_{xy}, \tau_{xz}), D_y = (\tau_{yx}, \tau_{yy}, \tau_{yz}), D_z = (\tau_{zx}, \tau_{zy}, \tau_{zz})$ are the strain terms and . The deterministic stress contribution is of the form:

$$Det_c = \begin{bmatrix} 0 \\ v_x' \left(\overbrace{(\rho \vec{v})} \cdot \vec{S} \right) \\ v_y' \left(\overbrace{(\rho \vec{v})} \cdot \vec{S} \right) \\ v_z' \left(\overbrace{(\rho \vec{v})} \cdot \vec{S} \right) \\ H' \left(\overbrace{(\rho \vec{v})} \cdot \vec{S} \right) \end{bmatrix} \tag{2-15}$$

and

$$\mathrm{Det}_v = \begin{bmatrix} \overline{D_x' . \vec{v}} \\ \overline{D_y' . \vec{v}} \\ \overline{D_z' . \vec{v}} \end{bmatrix} \cdot \vec{S} \tag{2-16}$$

To compute the stress terms and perform the model closure, a transport equation for the unsteady perturbations is obtained by retaining the first-order terms in the basic unsteady flow equations. Considering the first NN harmonic components of the periodic fluctuation U' U', a transport equation is obtained for each complex amplitude $\bar{U}_k \bar{U}_k$ of the fluctuation. By casting the 1st order linearized equation into the frequency domain, this harmonic perturbation equation is made space dependent only like the time-averaged flow equation. It can be made pseudo time dependent and, being in a conservative form, formulated following the finite-volume method:

$$\Omega_i \frac{d\tilde{U}}{dt_i} = - \sum_{\text{faces}} \tilde{F}_c \vec{S} + \sum_{\text{faces}} \tilde{F}_v \dot{S} + \Omega_i \tilde{S}_{Ti} \tag{2-17}$$

$$\tilde{F_c S} = \begin{bmatrix} \overbrace{(\rho \vec{v} . \vec{S})} \\ \overbrace{(\rho \vec{v} . \vec{S})} \widetilde{v_x} + \overbrace{(\rho \vec{v} . \vec{S})} \overline{v_x} + \tilde{p} S_x \\ \overbrace{(\rho \vec{v} . \vec{S})} \widetilde{v_y} + \overbrace{(\rho \vec{v} . \vec{S})} \overline{v_y} + \tilde{p} S_y \\ \overbrace{(\rho \vec{v} . \vec{S})} \widetilde{v_z} + \overbrace{(\rho \vec{v} . \vec{S})} \overline{v_z} + \tilde{p} S_z \\ \overbrace{(\rho \vec{v} . \vec{S})} \tilde{H} + \overbrace{(\rho \vec{v} . \vec{S})} \bar{H} \end{bmatrix} \tag{2-18}$$

$$\tilde{F}_v\vec{S} = \begin{bmatrix} 0 \\ \tilde{D}_x \cdot \vec{S} \\ \tilde{D}_y \cdot \vec{S} \\ \tilde{D}_z \cdot \vec{S} \\ (\tilde{B} \cdot \vec{S}) + \tilde{q} \end{bmatrix} \quad (2\text{-}19)$$

where

$$\tilde{B} = \begin{bmatrix} \bar{D}_x \cdot \tilde{\hat{v}} + \tilde{D}_x \cdot \tilde{\hat{v}} \\ \bar{D}_y \cdot \tilde{\hat{v}} + \tilde{D}_y \cdot \tilde{\vec{v}} \\ \bar{D}_z \cdot \tilde{\hat{v}} + \tilde{D}_z \cdot \tilde{\hat{v}} \end{bmatrix} \quad (2\text{-}20)$$

Besides the linearized terms of the Coriolis and centrifugal forces, the harmonic source term includes the complex term that was induced by the casting in the frequency domain:

$$\tilde{S_{T_k}} = -I\omega_k\tilde{U} \quad (2\text{-}21)$$

Propeller Performance Parameters

The propeller performance will be obtained as output from the numerical simulation in the form of Thrust (T) and Torque (Q). Meanwhile, the input parameters are airspeed (V), propeller diameter (D), and propeller rotational speed (n, in rotation per second). Those parameters can be defined in non dimensional parameters such as Advance Ratio (J) which is:

$$J = \frac{V}{nD} \quad (2\text{-}22)$$

Thrust and Power Coefficient is defined as:

$$C_T = \frac{T}{\rho n^2 D^4} \quad (2\text{-}23)$$

$$C_P = \frac{P}{\rho n^3 D^3} \quad (2\text{-}24)$$

Propeller power can be calculated from Torque:

$$P = 2\pi nQ \quad (2\text{-}25)$$

Propeller Efficiency can be calculated by the following equation:

$$\eta = \frac{T}{P}V = \frac{C_T}{C_P}J \quad (2\text{-}26)$$

3. Result and Analysis

There are 10 pairs of mode shapes and natural frequencies calculated which is analysed using coupled modal approach and nonlinear harmonics in NUMECA software. From the conducted simulations at three propeller angles 18°, 20°, and 22°, performance curves of the propeller were obtained. Each propeller angle was tested at five different RPM values, namely 1536, 1636, 1736, 1836, and 1936, with varying speeds for each RPM. These conditions are chosen based on the propeller operating conditions in the manual.

On each propeller angle, there are five performance curves, including the speed versus thrust curve, as shown in (Figure 3-1) to (Figure 3-3). In the three figures below, RPM 1936 exhibits the highest thrust value compared to the other four RPM values. Additionally, among all the simulated speeds, static speed conditions (zero airspeed) yield the highest thrust value for each RPM. At an angle of 18°, RPM 1736 and RPM 1636 have the same thrust value. This can be attributed to other factors such as airspeed, temperature, atmospheric pressure, and other environmental factors that can influence the propeller's performance. If these factors have a relatively constant influence on both RPM speeds, the speed versus thrust curve for both RPM values may exhibit a similar pattern. In all three figures, the thrust gradually decreases due to the presence of resistance and reaching the transition speed.

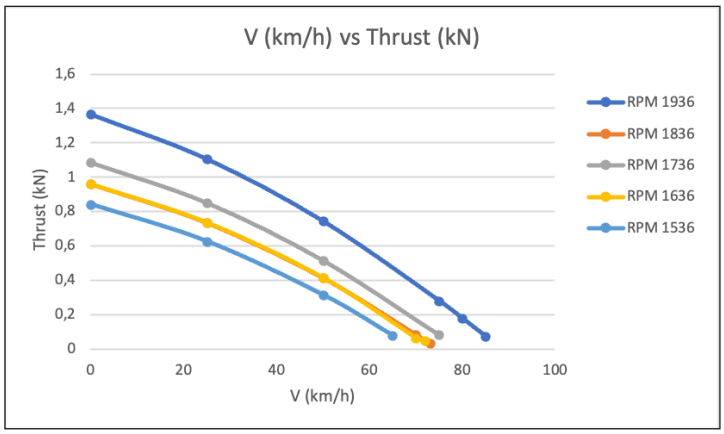


Figure 1-1: V (km/h) vs Thrust (kN) on angle 18°

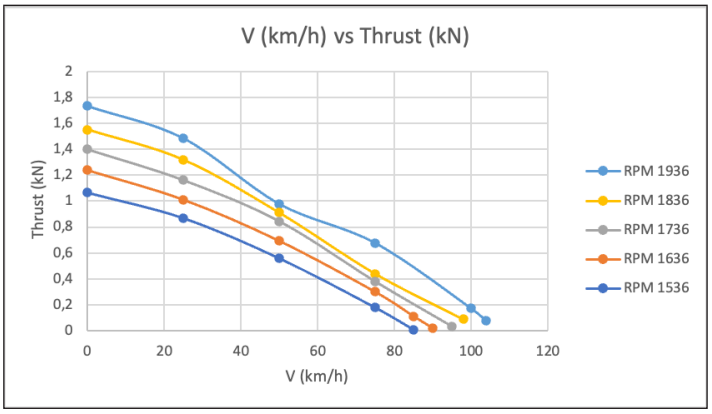


Figure 3-2: V (km/h) vs Thrust (kN) on angle 20°

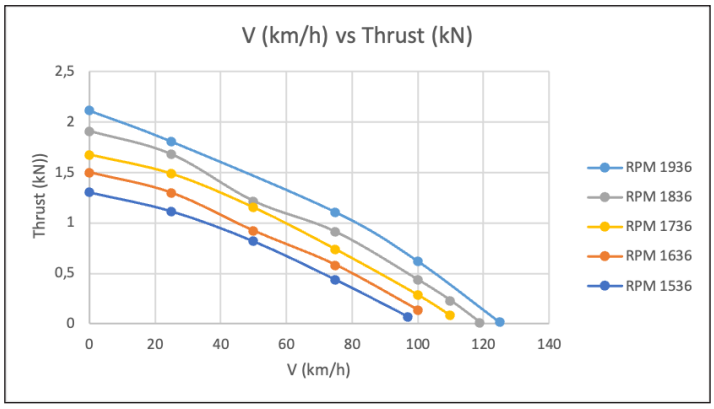


Figure 3-3: V (km/h) vs Thrust (kN) on angle 22°

The maximum propeller efficiency is achieved at an angle of 18° with RPM 1736 and a speed of 50 km/h, resulting in an efficiency value of 0.394. At an angle of 20°, the maximum efficiency occurs with RPM 1936 at a speed of 75 km/h, yielding an efficiency value of 0.582, as shown (Figure 3-4(to (Figure 3-6). Similarly, at an angle of 22°, the highest efficiency is attained with RPM 1936 and a speed of 75 km/h, resulting in an efficiency value of 0.675. These efficiency values are influenced by several factors, including the optimal angle of attack and power. At higher RPMs, the tip speed of the propeller increases. Higher tip speed results in faster airflow around the propeller, leading to improved aerodynamic efficiency. This is because propellers rotating at higher RPMs can achieve the optimal angle of attack to generate maximum lift force. Additionally, at higher RPMs, the power generated by the engine also increases. This greater power allows the propeller to operate at its optimal conditions, where it can produce higher thrust with greater efficiency, utilizing the energy provided by the engine more effectively.

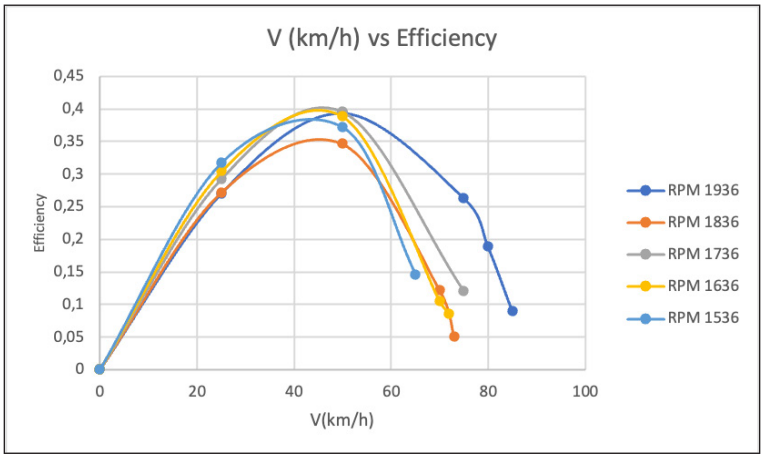


Figure 3 – 4: V (km/h) vs Efficiency on angle 18°

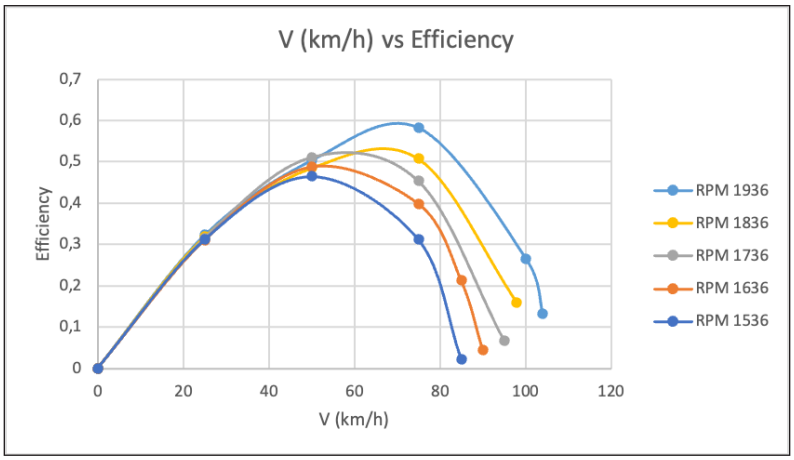


Figure 3-5: V (km/h) vs Efficiency on angle 20°

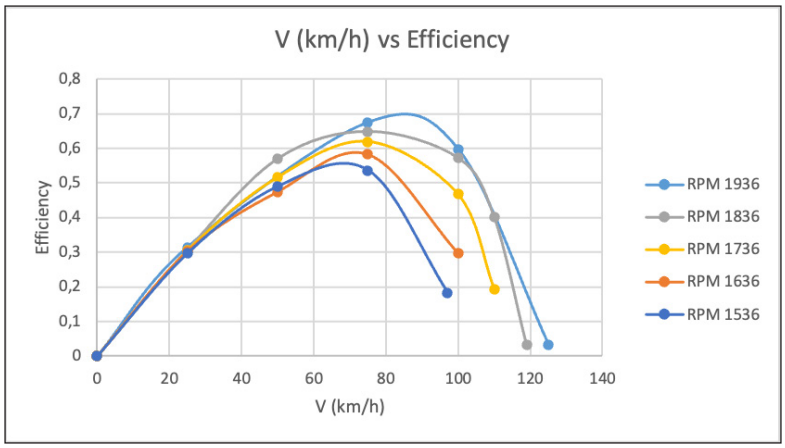


Figure 3-6: V (km/h) vs Efficiency on angle 22°

The value of advance ratio versus to cT changes as the advance ratio value varies, as shown in (Figure 3-7) to (Figure 3-9). At all five RPM values, the advance ratio values tend to be close to each other or compromise due to the influence of thrust values at each RPM. At low advance ratios (close to zero), the propeller can generate relatively high thrust compared to the power required. This indicates that the propeller is operating in a region where it efficiently converts power into thrust, resulting in a performance.

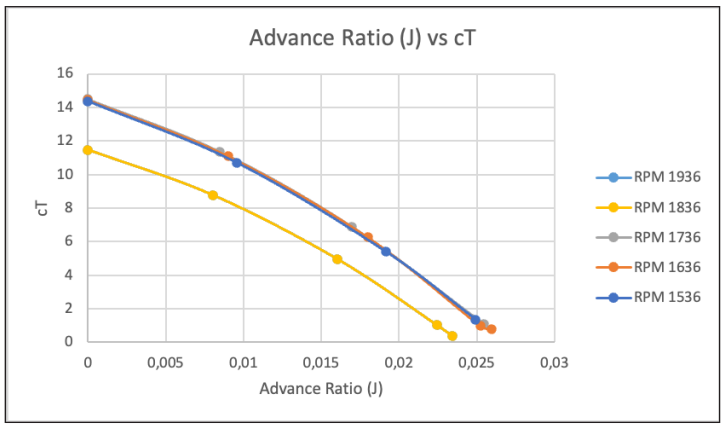


Figure 3-7: Advance Ratio (J) vs cT on angle 18°

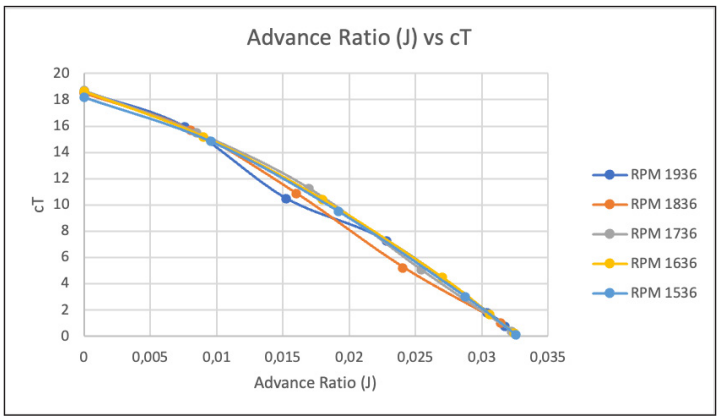


Figure 3–8: Advance Ratio (J) vs cT on angle 20°

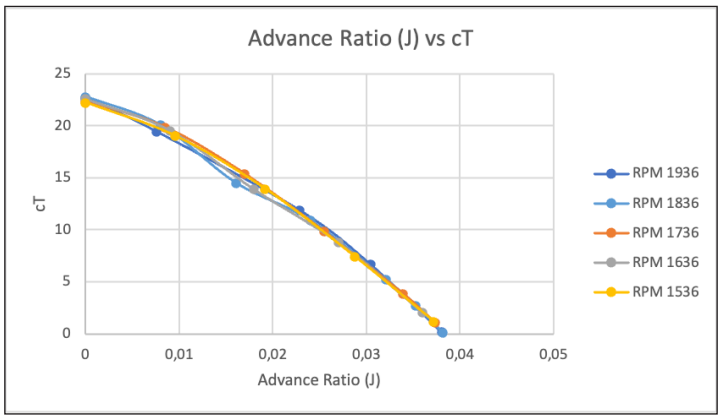


Figure 3-9: Advance Ratio (J) vs cT on angle 22°

The curve of advance ratio versus cP, the coefficient of power, changes as the advance ratio value varies. As shown in (Figure 3-10) to (Figure 3-12), the values of this curve are influenced by several factors, such as RPM, thrust, power, speed, and specifically, the propeller angle used. The five curves tend to converge or have values that are close to each other due to the influence of power values and propeller efficiency.

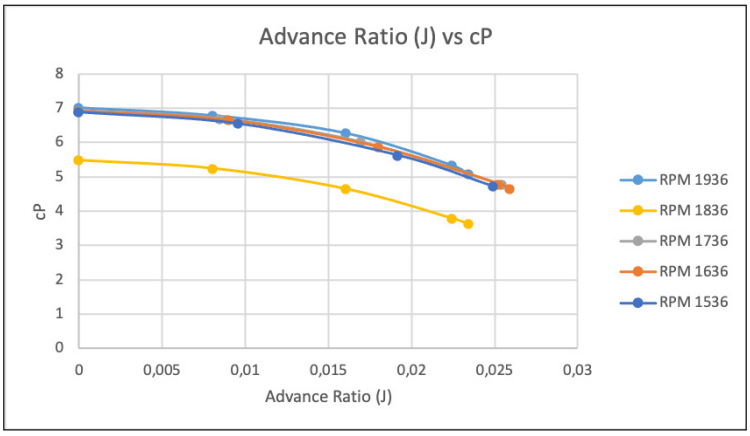


Figure 3-10: Advance Ratio (J) vs cP on angle 18°

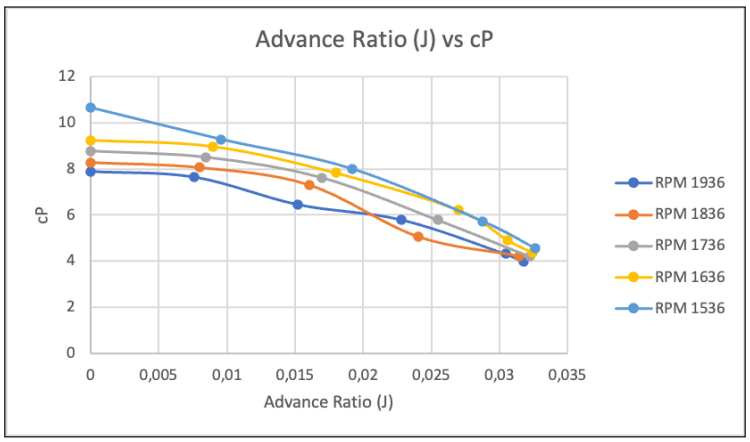


Figure 3-11: Advance Ratio (J) vs cP on angle 20°

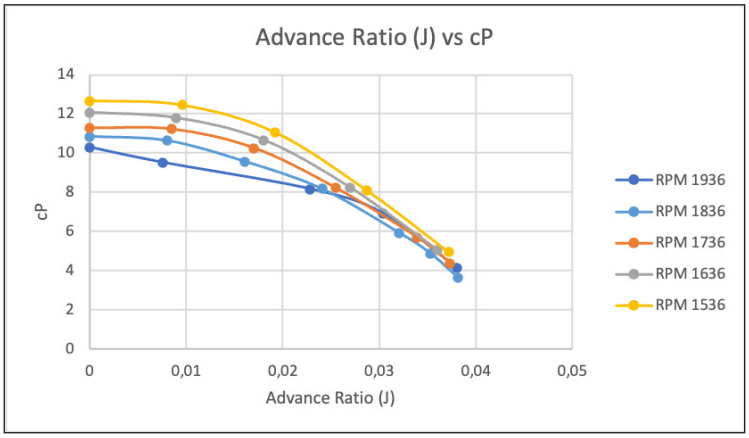


Figure 3-12: Advance Ratio (J) vs cP on angle 22°

The thrust and efficiency of a propeller depend on the propeller angle, RPM, and speed. A larger propeller angle will result in a higher thrust value, while higher RPM values closer to the propeller's maximum RPM will also yield higher thrust values. Additionally, speed affects both thrust and efficiency. As the speed increases, the thrust generated decreases gradually due to the drag phenomenon or resistance. Efficiency is dependent on the thrust value produced, as efficiency and thrust are directly proportional.

The advance ratio versus propeller efficiency relationship is influenced by the RPM and air speed values, which in turn affects thrust and power. As shown in (Figure 3-13) to 3-15), around the optimal advance ratio, the propeller reaches maximum efficiency, where a significant portion of the power delivered to the propeller is converted into useful output power. Across the five RPM values, the curves tend to converge or have values that are close to each other due to the compromise between propeller efficiency at each RPM value. The highest efficiency for each blade angle is shown in (Table 3-1).

Table 3-1: Maximum Efficiency for each blade pitch angle

Pitch angle (deg)	RPM	Advance Ratio, J	Efficiency
18	1736	0.0171	0.393
20	1936	0.0228	0.582
22	1936	0.0228	0.675

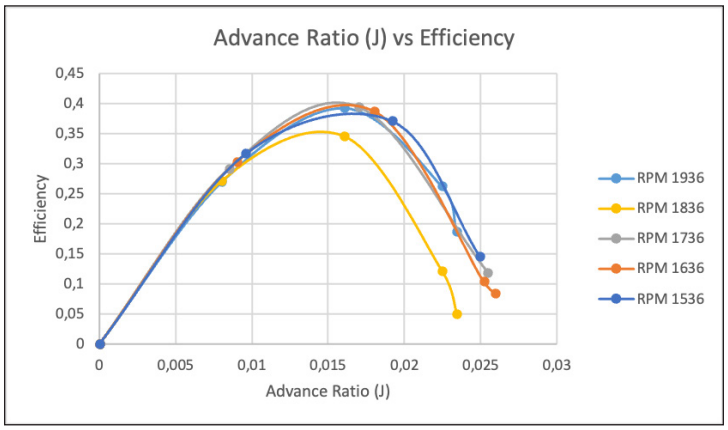


Figure 3-13: Advance Ratio (J) vs Efficiency on angle 18°

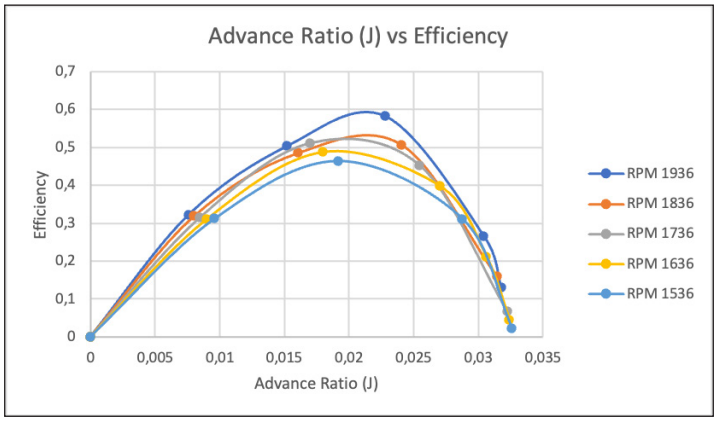


Figure 3–14: Advance Ratio (J) vs Efficiency on angle 20°

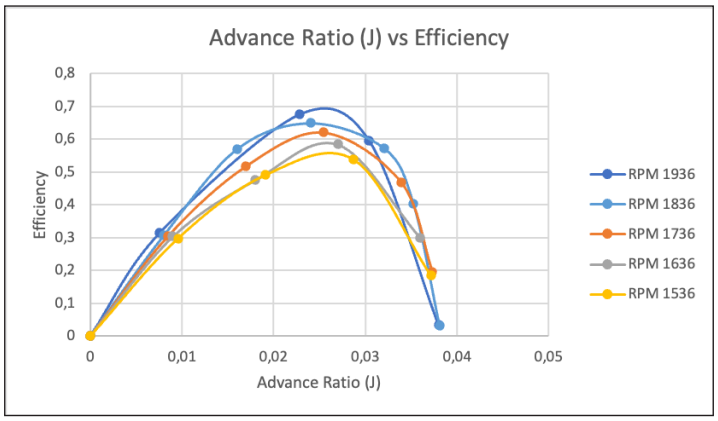


Figure 3–15: Advance Ratio (J) vs Efficiency on angle 22°

The propeller mode shape is shown in (Figure 3-16). Note that the deformation value acts like the amplitude that may scale uncontrollably if flutter happens.

The natural frequency and eigenvalue assigned for each mode shape is shown in (Table 3-2). Propeller operation in the natural frequencies and their multiplication will promote rapid increase in deformation.

Table 3-2: Natural frequency and eigenvalue for each mode shape

Mode Shape No.	Natural Frequency (Hz)	Eigenvalue
1	42.57	1.3978e-05
2	148.92	1.1421e-06
3	173.86	8.3798e-07
4	391.41	1.6534e-07
5	450.46	1.2483e-07
6	701.19	5.1519e-08
7	735.60	4.6812e-08
8	951.45	2.7981e-08
9	1097.37	2.1034e-08
10	1546.32	1.0594e-08

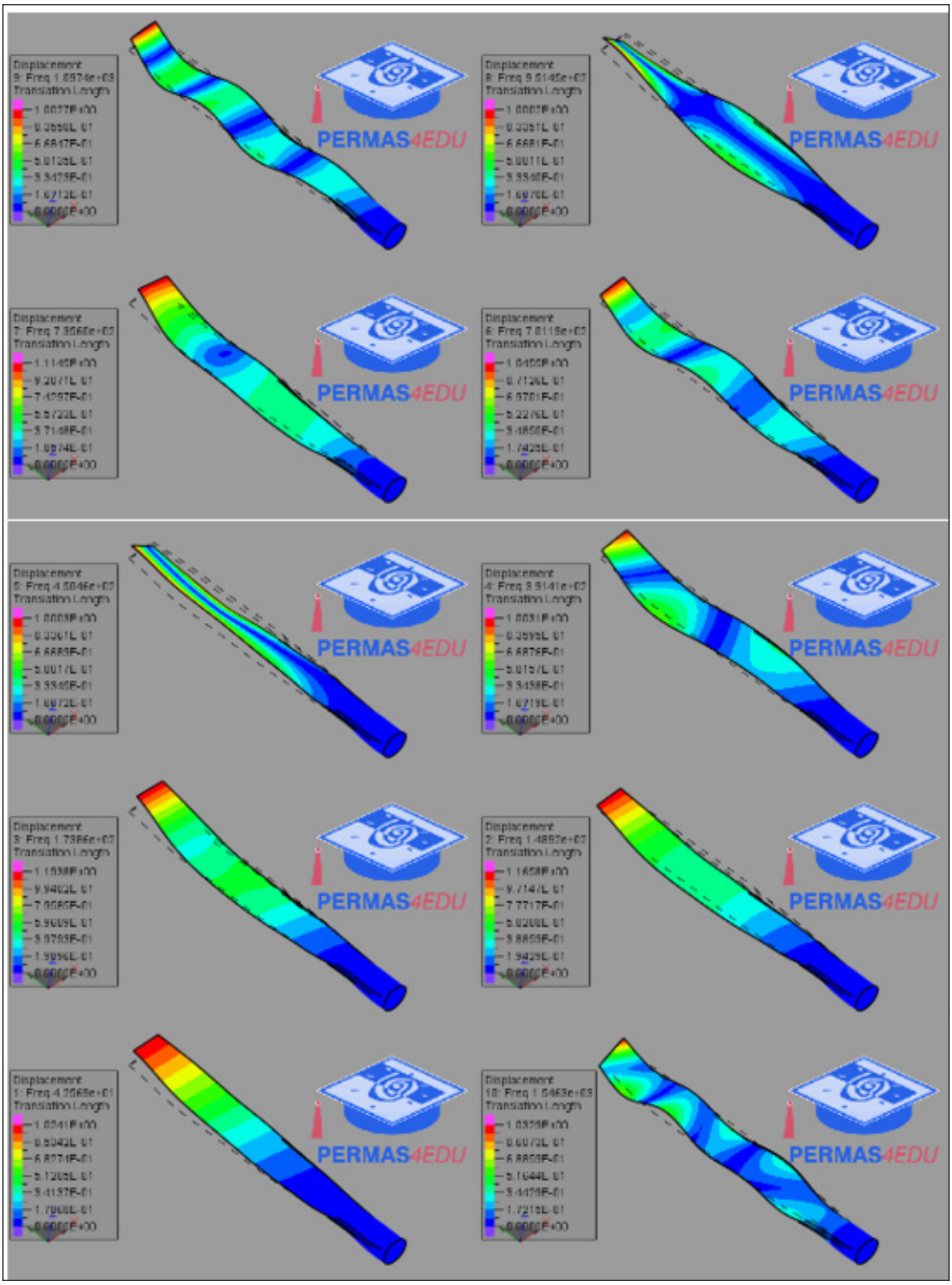


Figure 3-16: Propeller blade mode shapes 1 (top left) to 10 (bottom right)

The coupled modal approach and non-linear harmonic FSI results in blade maximum deformation over time as shown in (Figure 3-17) at the maximum efficiency nodes from each propeller pitch angle.. This indicates that vibrations occur, even though the deformations tend to be small. These continuous vibrations over a certain time range can affect the structural deformation of the propeller. The vibration characteristics are influenced by several factors, such as aerodynamics, the elastic properties of the material, and the impact of the RPM itself. The highest maximum deformation values for each angle are 0.183 mm, 0.185 mm, and 0.187 mm as shown in (Figure 3-17), while the maximum vibration velocity is 8.17 x 10^{-6} mm/s as shown in (Figure 3-18). It is shown that in the highest efficiency condition for each pitch angle, there are no rapid increase in deformation in a short time. In addition, according to Hartzell Propeller Owner's Manual No. 167 (Revision 6 dated September 2024 section "Maintenance Practices"), the lowest acceptable vibration level before the propeller needs to be dynamically balanced is 0.2 inches per second (IPS) or 5.08 mm/s, meaning the simulated propeller vibration can be considered safe in the operational conditions.

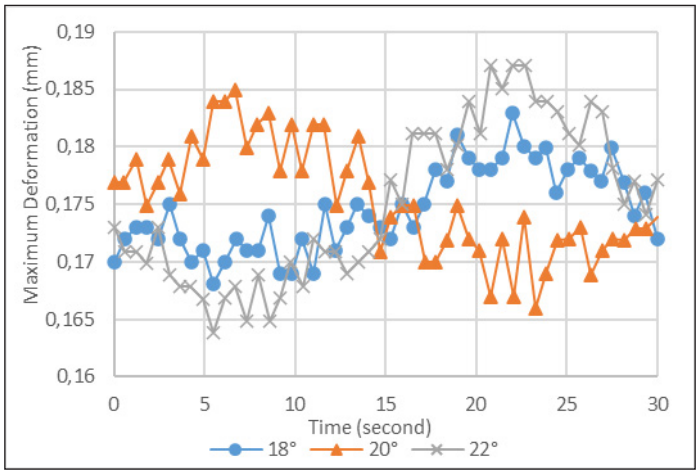


Figure 3-17: Blade deformation over time on various pitch angle

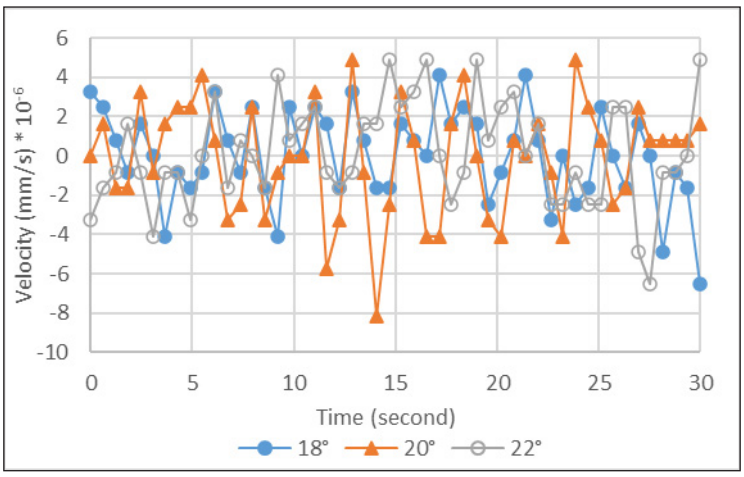


Figure 3-18: Vibration velocity over time on various pitch angle

4. Conclusions

The propeller performance is highly influenced by its operating condition. At low speed, propellers tend to generate the highest thrust and power value required to rotate the propeller.

Efficiency, however, is the lowest in static condition, then rises to its maximum value after which it falls drastically. The blade angle influences the maximum efficiency, which goes higher together with the blade angle value. This explains that the high blade angle is designed for higher aircraft speed. At the maximum efficiency settings for blade angle 18°, 20° and 22°, the blade deformation over time trend shows that there is no rapid increase in short time, which means the operating condition poses no flutter hazard. The vibration velocity is also much lower than the vibration tolerance imposed in the manual. While the simulation shows good results, the validation is only up to the methods used; experimental data is needed to confirm the vibration characteristics for this propeller.

5. Acknowledgements

The author would like to acknowledge the use of artificial intelligence (AI)-based tools in assisting with the formatting and organization of bibliographic references and in-text citations according to the APA 6th edition referencing style. All references and citations were subsequently reviewed and verified by the author, who remains fully responsible for their accuracy and appropriateness.

References

Muetze, A., & Strangas, E. G. (2016). The Useful Life of inverter-based drive bearings: Methods and research directions from localized Maintenace to prognosis. *IEEE Industry Applications Magazine*, *22*(4), 63–73. doi:10.1109/mias.2015.2459117

Maidi Saputra, & Hakim, I. (2018). Maintenance Propeller Hartzell Pada Pesawat Cessna 172. *Jurnal Mekanova Mekanikal Inovasi Dan Teknologi*, *2*(1). https://doi.org/10.35308/jmkn.v2i1.848

Min, B.-Y., Wake, B. E., Bowles, P. O., C.G. Matalanis, & Moffitt, B. (2015). *Propeller Analysis using a Hybrid Navier-Stokes/Free-Wake Method*.

Czyż, Z., Karpiński, P., Skiba, K., & Wendeker, M. (2021). Wind Tunnel Performance Tests of the Propellers with Different Pitch for the Electric Propulsion System. *Sensors*, *22*(1), 2. https://doi.org/10.3390/s22010002

Higgins, R. J., Jimenez-Garcia, A., Barakos, G. N., & Bown, N. (2019). High-Fidelity Computational Fluid Dynamics Methods for the Simulation of Propeller Stall Flutter. AIAA Journal/AIAA Journal on Disc, 57(12), 5281–5292. https://doi.org/10.2514/1.j058463

Higgins, R., Jimenez-Garcia, A., Barakos, G. N., & Bown, N. (2019). A Time-Marching Aeroelastic Method Applied to Propeller Flutter. *AIAA SCITECH 2022 Forum*. https://doi.org/10.2514/6.2019-1102

Zhu, W., & Gao, H. (2019). A Numerical Investigation of a Winglet-Propeller Using an LES Model. *Journal of Marine Science and Engineering*, *7*(10), 333. https://doi.org/10.3390/jmse7100333

Prasad, A. S., Ramakrishna, S., & M. Madhavi. (2018). *Experimental Investigations on Static and Dynamic Parameters of Steel and Composite Propeller Shafts with an Integrated Metallic Joints*. *5*(13), 26925–26933. https://doi.org/10.1016/j.matpr.2018.08.180

Prasad L, M., Manjunath, Sathish, & Kumar, S. (2018). Structural and Vibration Analysis of propeller blade in small aircraft. *International Research Journal of Engineering and Technology (IRJET)*, *5*(11), 595–600. https://www.irjet.net/archives/V5/i11/IRJET-V5I11117.pdf

Ghalamchi, B., Jia, Z., & Mueller, M. W. (2020). Real-Time Vibration-Based Propeller Fault Diagnosis for Multicopters. *IEEE/ASME Transactions on Mechatronics*, *25*(1), 395–405. https://doi.org/10.1109/tmech.2019.2947250

Qu, Y., Su, J., Hua, H., & Meng, G. (2017). Structural vibration and acoustic radiation of coupled propeller-shafting and submarine hull system due to propeller forces. *Journal of Sound and Vibration*, *401*, 76–93. https://doi.org/10.1016/j.jsv.2017.03.034

Ruseno, N. (2024). FEM Modal Analysis of Blades Number Effect in UAV Propellers. Indonesian Journal of Aerospace, 22(1), 1–12. https://doi.org/10.55981/ijoa.2024.39

Prabhu, J. J., Dash, A. K., Nagarajan, V., & Sunny, M. R. (2022). Vibration analysis of cycloidal propeller blade during ship maneuvering. *Journal of Marine Science and Technology*, *28*(1), 44–71. https://doi.org/10.1007/s00773-022-00899-1

J. H. Mak and W. S.-I. W. Salim, Analysis of propeller blade through CFD modelling. Journal of Design for Sustainable and Environment. Vol. 4 No. 1 (2022) p. 25–31.

Ji, Z., Guo, T., Zhou, Di, Lu, Z., & Lyu, B. (2024). Time-Domain Analysis of Body Freedom Flutter Based on 6DOF Equation. *Computer Modeling in Engineering & Sciences*, *138*(1), 489–508. https://doi.org/10.32604/cmes.2023.029088

Drachinsky, A., Avin, O., Raveh, D. E., Yaron Ben-Shmuel, & Tur, M. (2022). Flutter Tests of the Pazy Wing. *AIAA Journal*, *60*(9), 5414–5421. https://doi.org/10.2514/1.j061717

Hartzell Propeller LLC. (2024). *Propeller owner's manual and logbook: Steel hub reciprocating propellers with aluminum blades* (Manual No. 167, 61-00-67, Rev. 6). Piqua, OH: Author.